

30. For Gaspra, see P. Helfenstein *et al.*, *Icarus* **107**, 37 (1994). For Ida, see J. Veverka *et al.*, *Icarus* **120**, 66 (1996).

31. Using the size of Eros determined from NEAR observations (Table 1) and published values of the photometric parameters *H* and *G* for Eros, the range of values for the geometric albedo in the V band is 0.15 to 0.32.

32. W. Wisniewski, *Icarus* **28**, 87 (1976).

33. H. Larson *et al.*, *Icarus* **28**, 95 (1976).

34. S. M. Murchie and C. M. Pieters, *J. Geophys. Res.* **101**, 2201 (1996).

35. For disk-resolved measurements in approach imaging, scattered-light removal techniques were applied to remediate the effects of contaminants accumulated on the outer optics after the NEAR anomaly on 20 December 1998. In summary, the Fourier transform of an image is divided by the Fourier transform of the point-spread function (PSF) plus a noise term. The inverse of the quotient provides a scattered-light remediating image.

36. For whole-disk color measurements, all signal within a box surrounding Eros was summed to include all scattered light. Spectra were scaled to unity at a reference wavelength of 550 nm. An upper limit to the uncertainties in relative spectra was obtained by

comparing spectra from similar views of the asteroid acquired close in time. This procedure provides an upper limit on actual uncertainties because it incorporates both measurement errors and any real spectral differences.

37. F. Vilas and L. McFadden, *Icarus* **100**, 85 (1992).

38. For example, B. Hapke and H. Van Horn, *J. Geophys. Res.* **15**, 4545 (1963); J. B. Adams and A. L. Felice, *J. Geophys. Res.* **72**, 5705 (1967); W. G. Egan *et al.*, *Icarus* **19**, 358 (1973).

39. T. Gehrels *et al.*, *Astron. J.* **75**, 186 (1970).

40. The phase coefficient is defined as the slope of the phase curve (plotted on a magnitude scale). See J. Veverka, in *Physical Studies of Minor Planets*, T. Gehrels, Ed., *NASA Spec. Publ. SP-267*, 91 (1971), p. 91; J. Gradie and J. Veverka, *Proc. Lunar Planet. Sci.* **13**, 1769 (1981).

41. The NIS data are compared with a phase curve at visible wavelengths (550 nm) generated by fitting a photometric model to all available visible-light, whole-disk observations of Eros (both telescopic and NEAR).

42. N. I. Izenberg *et al.*, *Icarus*, in press. To generate this average spectrum, raw NIS measurements were calibrated to *I/F*, and instrument pointing and NEAR trajectory information were used to eliminate spec-

tra for which the NIS aperture did not fall entirely on the asteroid, thus avoiding spurious instrumental effects. Spectra exhibiting saturation or *I/F* values below a threshold value (10%) were also eliminated.

43. C. R. Chapman and D. Morrison, *Icarus* **28**, 91 (1976).

44. M. J. Gaffey *et al.*, in *Asteroids II*, R. P. Binzel *et al.*, Eds. (Univ. of Arizona Press, Tucson, AZ, 1989), pp. 98–127.

45. M. J. Gaffey *et al.*, *Icarus* **106**, 573 (1993).

46. For example, C. M. Pieters *et al.*, *J. Geophys. Res.* **98**, 20817 (1993).

47. C. M. Pieters, *J. Geophys. Res.* **88**, 9534 (1983).

48. J. Trombka, private communication. For a description of the XRS experiment, see J. Trombka *et al.*, *J. Geophys. Res.* **102**, 23729 (1997).

49. J. Veverka *et al.*, *J. Geophys. Res.* **102**, 23709 (1997).

50. We thank the Mission Design, Mission Operations, and Spacecraft teams of the NEAR Project at the Applied Physics Laboratory of Johns Hopkins University for their dedicated and successful efforts that resulted in making NEAR the first-ever orbiter of an asteroid. We also express our gratitude to R. Binzel and to an anonymous referee for helpful and constructive reviews.

25 May 2000; accepted 11 August 2000

The Shape of 433 Eros from the NEAR-Shoemaker Laser Rangefinder

Maria T. Zuber,^{1,2*} David E. Smith,² Andrew F. Cheng,³ James B. Garvin,² Oded Aharonson,¹ Timothy D. Cole,³ Peter J. Dunn,⁴ Yanping Guo,³ Frank G. Lemoine,² Gregory A. Neumann,^{1,2} David D. Rowlands,² Mark H. Torrence⁴

Measurements from the Near Earth Asteroid Rendezvous (NEAR)–Shoemaker Laser Rangefinder (NLR) indicate that asteroid 433 Eros is a consolidated body with a complex shape dominated by collisions. The offset between the asteroid’s center of mass and center of figure indicates a small deviation from a homogeneous internal structure that is most simply explained by variations in mechanical structure. Regional-scale relief and slope distributions show evidence for control of topography by a competent substrate. Impact crater morphology is influenced by both gravity and structural control. Small-scale topography reveals ridges and grooves that may be generated by impact-related fracturing.

The sizes and shapes of asteroids contain information about the thermal, collisional, and dynamical histories of these bodies, many of which are remnants of the materials from which the solar system accreted. Some analyses (1, 2) have proposed that for all but the handful of largest asteroids, shape is controlled by collisions, with only a minor contribution from self-gravitation. However, oth-

er analyses (3, 4) have favored the hypothesis (5) that asteroids are rubble piles, i.e., aggregates held together by gravitational attraction rather than material strength. The geometries of impact structures on all but the smallest (100 m to 1 km) asteroids are also thought to be dominated by gravity (6–9). Precise measurements of topography at a range of spatial scales now enable the influences on an asteroid’s collisional history to be quantitatively established.

The NEAR-Shoemaker spacecraft is currently in orbit about the near-Earth asteroid 433 Eros and is performing systematic global mapping at varying orbital altitudes. During elliptical and circular orbit phases of the NEAR mission (10, 11), the NLR (12–14) has so far collected ~8 million measurements of the range from the spacecraft to the aster-

oid (Fig. 1) (15). From these data we have constructed a topographic model of Eros (Fig. 2) with a spatial resolution of 960 m and a radial accuracy of ~30 m (16) with respect to the asteroid’s center of mass (17).

Eros has a mean radius of 7311 ± 10 m (Table 1) and exhibits excursions in the equatorial plane that range from ~3500 m to over 17,500 m. The maximum chord is 32.697 km (oriented along 3.96°N, 185.47°E to 0.31°S, 18.69°E), consistent with an orbital value of 31.4 km based on imaging (18) and with a ground-based estimate of 36 km derived from analysis of radar echo spectra (19).

The best-fit ellipsoid (Table 2) fits the observed shape with a root mean square (rms) of 1028 m. Compared with other asteroids and small moons imaged by spacecraft or for which stellar occultation limb profiles are available (20), Eros’s deviation of nearly 60% from its ellipsoidal radius represents a poor fit to an ellipsoid. However, at least some of the variance may be a consequence of the high spatial resolution of our topographic model, which accentuates departures from simple shapes. While Eros’s shape deviates from an ellipsoid, the asteroid shows no evidence of a dumbbell shape that would suggest a contact binary bound loosely by self-gravitation as observed for some asteroids (21, 22).

Moments derived from the shape model assuming a constant-density interior [Web table 1 (23)] indicate that Eros has a stable rotation. The extent to which a constant-density interior is characteristic of the asteroid can be quantified to first order from the offset between the center of mass (COM) and center of figure (COF), which is indicative of density inhomogeneities within the body. For an object in a mass-centered coordinate system, the COF is equivalent to the COM of an identical object of homogeneous density

¹Department of Earth, Atmospheric, and Planetary Sciences, Massachusetts Institute of Technology, Cambridge, MA 02139, USA. ²Earth Sciences Directorate, NASA–Goddard Space Flight Center, Greenbelt, MD 20771, USA. ³Johns Hopkins University Applied Physics Laboratory, Laurel, MD 20723–6099, USA. ⁴Raytheon Information Technology and Scientific Services, Landover, MD 20771, USA.

*To whom correspondence should be addressed. E-mail: zuber@mit.edu

REPORTS

(24). The COM/COF offset on Eros (Table 1 and Web fig. 1) reveals a small departure from homogeneity, most pronounced along the Z and X axes. Any inversion for the internal density distribution from topography and gravity is inherently nonunique, but it is illustrative to consider a simple scenario for the density structure required to match the observed offset. For a linearly varying density distribution, the gradient required for the COM/COF offset to vanish is $\sim 6.0 \text{ kg m}^{-3} \text{ km}^{-1}$. This density gradient can be interpreted in terms of a hemispheric-scale difference in the thickness of regolith, i.e., the unconsolidated, impact-generated surface layer. If the upper limit of the density of Eros's regolith is similarly less (66%) than its bulk rock equivalent on the moon (25), then the COM/COF offset can be explained by a regolith layer in the direction of the COF (26) with a maximum thickness of $\sim 100 \text{ m}$ that overlies consolidated basement. In this simplified scenario the thickness of the regolith in the

hemisphere opposite the COF is zero. However, more complex and realistic distributions are also possible. For example, if Eros's regolith is less dense than the maximum density of lunar regolith, or if bedrock is fractured (26), then smaller regolith thickness differences between the hemispheres are implied. A globally averaged regolith thickness on the order of 10^2 m has been suggested for some asteroids on the basis of collision models (4, 27), experiments (3, 28), and radar backscatter measurements (22), and the heterogeneity of Eros's internal density distribution is compatible with such estimates. Considering the evidence for global homogeneity in surface composition from the NEAR-Shoemaker XGRS instrument (29), we suggest that the COM/COF offset is most easily explained by small variations in Eros's internal mechanical structure rather than in subsurface composition. If instead Eros contains lateral variations in internal composition consistent with the range of measured densities of probable

meteorite analogs (26), then any sizable variations in regolith distribution are disallowed. We believe that such a scenario is unlikely.

Other major features of Eros's long-wavelength shape are two large concavities (Figs. 2 and 3). One structure consists of an $\sim 4\text{-km}$ -wide closed cavity in the region 20°N , 240°E to 290°E that has been provisionally named Psyche. On the basis of its central depression and bounding partial rim, we interpret this structure to be an impact crater. The bottom of Psyche (13.5°N , 273.5°E) contains the smallest radius on Eros, $2939 \pm 30 \text{ m}$. The difference in elevation between the lowest point in the floor and the highest closed contour is 1800 m . This relief can be interpreted as the depth, but the value is

Table 1. 433 Eros geodetic parameters from NLR190 shape, gravity, and dynamics model.

Parameter	Value	Uncertainty
Mean radius, C_{00} (m)	7,311	± 10
Mean equatorial radius (m)	9,236	± 100
North polar radius (m)	5,338	± 50
South polar radius (m)	5,993	± 50
Maximum equatorial radius (m)	17,542	± 50
Minimum equatorial radius (m)	3,501	± 50
Volume (km^3)	2,505	± 100
<i>Topography</i>		
Normalized spherical harmonic coefficients (m)		
$C_{1,0}$	-133	± 10
$C_{1,1}$	136	± 10
$S_{1,1}$	593	± 10
$C_{2,0}$	-1,092	± 10
$C_{2,1}$	-42	± 10
$S_{2,1}$	51	± 10
$C_{2,2}$	2,120	± 10
$S_{2,2}$	-891	± 10
Offset of COF from COM (m)*		
Δx	-28	± 20
Δy	-4	± 20
Δz	14	± 20
Direction of rotation axis		
Right ascension (deg.)	11.38	± 0.01
Declination (deg.)	17.18	± 0.01
Rotation		
$\dot{\theta}$ (deg./day)	1,639.390	± 0.002
Ω_0 (deg.)	361.6	± 10.0
<i>Gravity field</i>		
Normalized spherical harmonic coefficients		
$C_{2,0}$	-0.05210	± 0.00008
$C_{2,1}$	0.00000	± 0.00005
$S_{2,1}$	-0.00020	± 0.00005
$C_{2,2}$	0.04890	± 0.00714
$S_{2,2}$	0.13170	± 0.02220
$C_{3,0}$	-0.00180	± 0.00027
$C_{3,1}$	0.00600	± 0.00044
$S_{3,1}$	0.00080	± 0.00053
$C_{3,2}$	-0.00010	± 0.00062
$S_{3,2}$	-0.00690	± 0.00144
$C_{3,3}$	-0.03220	± 0.00463
$S_{3,3}$	0.00560	± 0.00383

*From numerical integration of shape model.

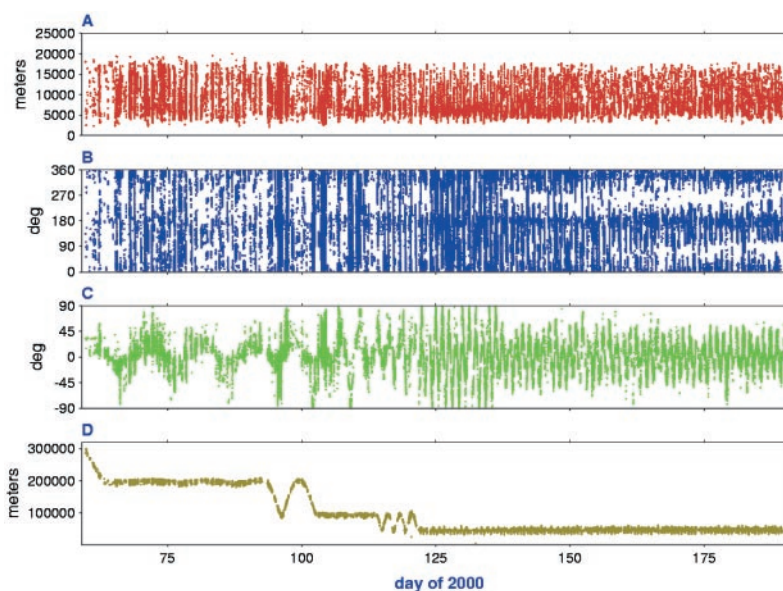
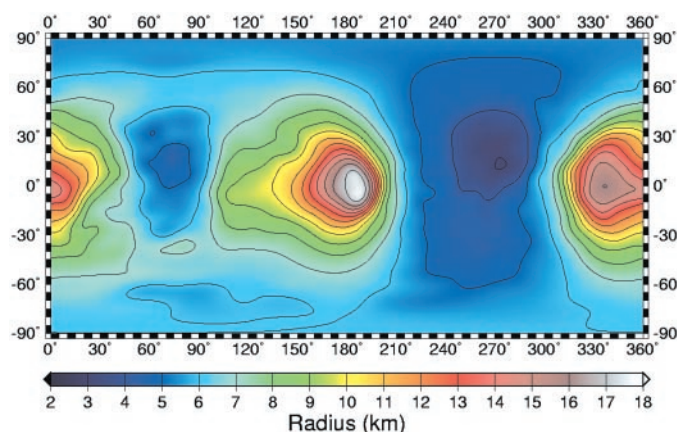


Fig. 1. Time history of NLR observations of 433 Eros at individual laser bounce used in the analysis (39). (A) Radius; (B) longitude; (C) latitude; (D) range from NEAR-Shoemaker spacecraft to the surface of the asteroid.

Fig. 2. Map view of the radius of Eros in cylindrical projection. This analysis uses a planetocentric coordinate convention with east positive longitude. One degree of latitude on Eros ranges from ~ 54 to 307 m . The regional low at 90°E is Himeros and that at 270°E is Psyche.



REPORTS

poorly constrained because the structure is situated within a regional low. Even given the depth uncertainty, Psyche is deeper relative to its size than simple (bowl-shaped) craters

on the terrestrial planets, consistent with its formation in a low-gravity and perhaps a low-velocity regime.

A second, larger concavity, provisionally

named Himeros, is centered at 0°N, 75°E. This structure spans a distance on the surface of slightly greater than Eros's mean radius and displays a saddle shape (Fig. 3), with the symmetry axis of its broad inflection in curvature [Web fig. 2 (23)] oriented approximately longitudinally. The structure also exhibits complex short-wavelength curvature variations to the east and west of the structure that trend approximately latitudinally. Himeros lacks topographic characteristics that are commonly associated with an impact origin such as a closed depression, rim, and ejecta blanket (20, 30, 31). If Himeros's present morphology was preserved since its time of formation, then this feature likely formed as a consequence of collision, i.e., contact between two bodies of roughly similar sizes. However, at the current resolution of the topographic model we cannot rule out the possibility that this structure formed as a result of impact when Eros was part of a larger parent body, or during the process of the asteroid's breakaway into a separate entity. In either of these scenarios, the morphology of an originally impact-generated Himeros would have been modified from its original configuration. We see no geophysical evidence that would suggest that Eros attained its present shape by accumulation or reaccumulation of smaller asteroidal bodies.

A mesh view of the shape of Eros (Fig. 4A) in the vicinity of Himeros includes superposed vectors of gravitational acceleration (32) that indicate directions of downslope movement. The highest slopes on the asteroid cluster to the southwest and northwest of Himeros, which are regions that have lower than average crater density (18), and collectively suggest that these are regions where regolith has been transported downward (with respect to the gravitational potential) by mass wasting.

The histogram in Fig. 4B shows that the average slope on a surface baseline of ~3° is about 10°, substantially higher than that on a comparable spatial scale on the terrestrial plan-

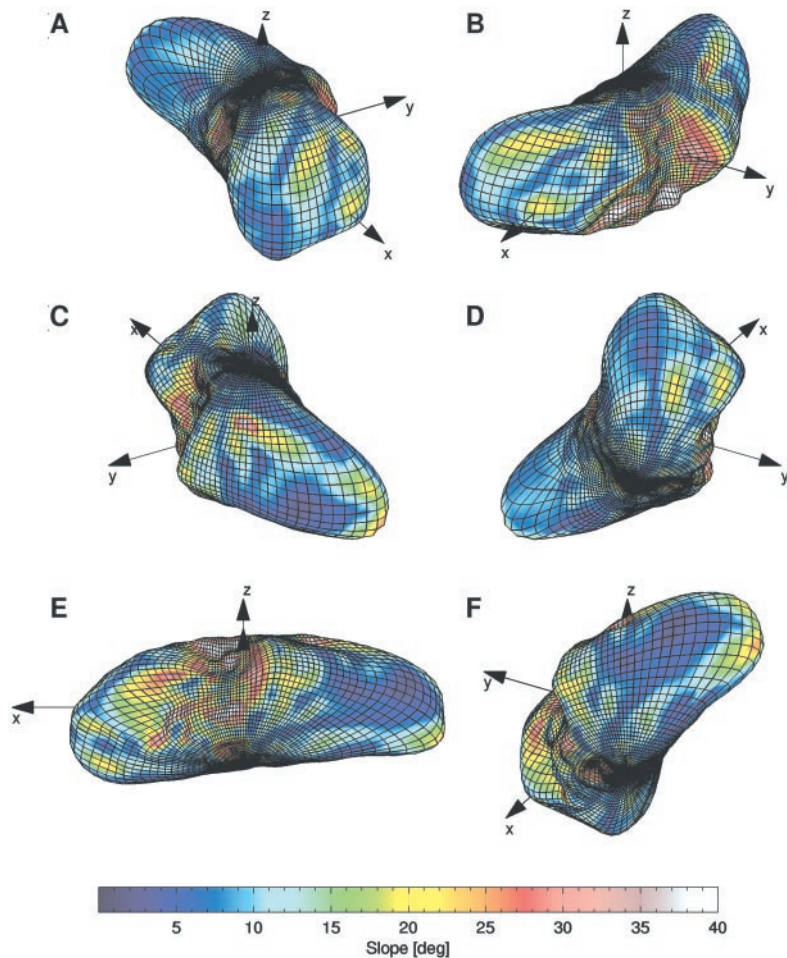


Fig. 3. Six perspective views of a three-dimensional shape model of 433 Eros from the NLR plotted to spherical harmonic degree and order 24. The mesh represents the scaled shape, and the surface facets are color-coded according to the surface slope with respect to a constant-density gravity field derived from the shape model (32). The asteroid is viewed at the following (elevation, azimuth) pairs: (A) 30°N, 60°E; (B) 30°N, 120°E; (C) 30°N, 0°E; (D) 30°S, 60°E; (E) 30°S, 300°E; and (F) 30°S, 0°E.

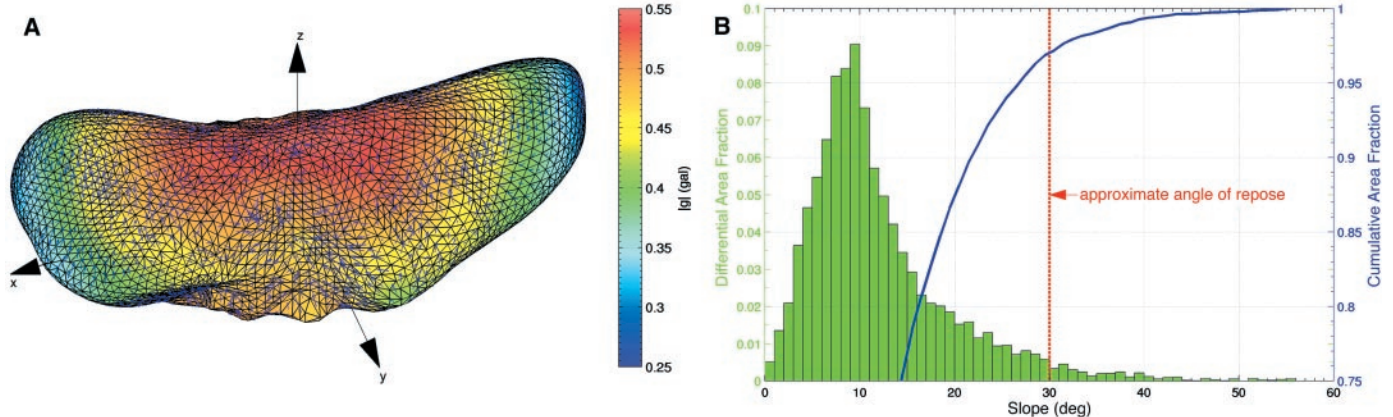


Fig. 4. (A) Vectors showing directions of gravitational acceleration (\vec{g}). Units are Gals, where 1 Gal = 1 cm s⁻². The asteroid is viewed from 30°N, 60°E. Colors represent the magnitude of \vec{g} and arrows indicate the direction. (B) Histogram and cumulative frequency distribution of 3°-baseline surface slopes (32).

Fig. 5. NLR altimetric profile collected on day 116 showing elevation as a function of time (in seconds). A linear trend in the radius has been removed to accentuate small-scale relief. Impact craters can be seen at 4900 and 7800 s, and grooves are visible in the intervals 6000 to 6800 s and 8900 to 9100 s. The vertical exaggeration is about 6:1.

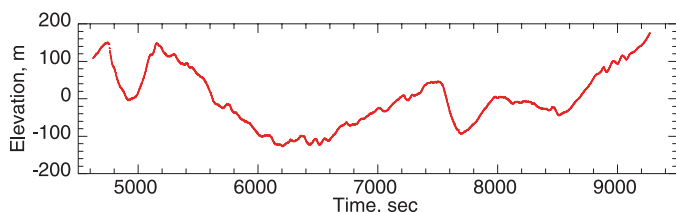


Table 2. 433 Eros triaxial ellipsoid parameters.

Parameter*	Value	Uncertainty
<i>Triaxial ellipsoid</i>		
a (m)	20591	±40
b (m)	5711	±40
c (m)	5332	±50
<i>Ellipsoid offset of COF from COM</i>		
Δx (m)	470	±20
Δy (m)	720	±20
Δz (m)	-202	±30
<i>Direction of ellipsoidal axes†</i>		
a (lat/lon E), deg.	0/349	±5
b (lat/lon E), deg.	82/259	±5
c (lat/lon E), deg.	8/259	±5

*Derived from a fit to the 24 by 24 spherical harmonic model NLR190. † Estimates of the directions of the axes are inaccurate because of the inherent deviation in asteroid shape from a triaxial ellipsoid. Results suggest that the major axis (a) is ~11° away from the X axis of the coordinate system and the "polar" axis (b) is about 8° from the Z axis.

ets. About 4% of these slopes exceed the approximate angle of repose (~30°), defined as the maximum angle for which unconsolidated material could remain on that surface. The highest slopes on the asteroid are clustered on the peripheries of Himeros and Psyche, which suggests that in these regions hundred-meter-scale relief reflects a competent substrate. Higher than average slopes also cluster to the southwest of Psyche, to the east and west of Himeros, and near the pointed edge of the asteroid at longitude 180°E. Regions in the vicinity of Psyche and Himeros (270°E, 75°E) are areas of relatively large inward-directed gravitational acceleration, whereas near the ends of the asteroid (0°E, 180°E) the outward-directed centrifugal force nearly counterbalances the attraction due to the mass distribution. Near the ends of Eros \vec{g} is about a factor of 2 lower than in areas of small radii (Fig. 4A) (11). Thus, the emplacement and redistribution of regolith on Eros is expected to be heterogeneous, although Figs. 3 and 4 indicate that downslope movement of regolith could be possible in both high- and low- \vec{g} regions, with different efficiency.

Topographic profiles sampled the roughness and relief of the asteroid at the scale of the laser footprint. An NLR profile that subtends about 90° of longitude and about 10 km of distance (Fig. 5) shows grooves that are also visible in images (18). Structures mea-

sured by the NLR have a width of about 70 to 120 m and a vertical scale of 5 to 25 m. Grooves may be the surface manifestation of penetrative fracturing (9, 33), plausibly a consequence of stresses produced by impact.

The NLR has sampled impact craters at varying spatial scales over the surface of Eros. Cross sections across numerous small craters have been obtained, such as two examples in Fig. 5. In addition, structures of several-hundred-meter scale and larger are resolved in the global grid. Although geometric parameters have yet to be systematically quantified, existing measurements show that craters of 10²- to 10³-km scale often display subdued rims, such as Psyche, or are rimless (Fig. 5). If near-surface material on Eros is not capable of plastic deformation, then crater rims indicate formation in a gravity-controlled regime, consistent with the predictions from collision and cratering models of silicate-rich asteroids in Eros's size range (6-9). Poorly developed rims may be a consequence of asteroidal erosion processes, such as ejecta mantling from nearby impacts or mass wasting, the latter perhaps enhanced by elastic waves generated by other impacts. However, subdued and especially missing rims may also reflect the influence of target strength on crater geometry. A number of large craters exhibit angularity in three-dimensional relief, such as shown in the regional elevation model of a crater near Eros's north pole in Web fig. 3 (23), which provides further support for the notion of structural influence on crater geometry. The combination of Eros's bulk density and inferred deviations from internal homogeneity, clustered regions of high slopes, craters with poorly developed rims or that lack rims and exhibit polygonal planform, and long, continuous grooves of finite depth collectively represent evidence for structural competence. Crater rims, bowl-shaped crater depressions, regolith, and zones of mass wasting constitute evidence for gravitational control. Thus, both mechanical strength and gravity have demonstrably influenced the evolution of Eros.

References and Notes

1. J. F. Bell, D. R. Davis, W. K. Hartmann, M. J. Gaffey, in *Asteroids II*, R. P. Binzel, T. Gehrels, M. S. Matthews, Eds. (Univ. of Arizona Press, Tucson, AZ, 1989), pp. 921-945.
2. V. Catullo, V. Zappala, P. Farinella, P. Paolicchi, *Astron. Astrophys.* **138**, 464 (1984).

3. E. V. Ryan, W. Hartmann, D. Davis, *Icarus* **94**, 283 (1993).
4. H. J. Melosh and E. V. Ryan, *Icarus* **129**, 562 (1997).
5. D. R. Davis, C. R. Chapman, R. Greenberg, S. J. Weidenschilling, in *Asteroids*, T. Gehrels, Ed. (Univ. of Arizona Press, Tucson, AZ, 1979), pp. 528-557.
6. E. Asphaug *et al.*, *Icarus* **120**, 158 (1996).
7. S. J. Love and T. J. Ahrens, *Icarus* **124**, 141 (1996).
8. M. C. Nolan, A. Asphaug, H. J. Melosh, R. Greenberg, *Icarus* **124**, 359 (1996).
9. E. Asphaug and H. J. Melosh, *Icarus* **101**, 144 (1993).
10. A. F. Cheng *et al.*, *J. Geophys. Res.* **102**, 23695 (1997).
11. D. K. Yeomans *et al.*, *Science* **289**, 2085 (2000).
12. The NLR (14), designed and built at the Johns Hopkins University Applied Physics Laboratory, is a direct-detection laser radar. The laser transmitter, built by McDonnell-Douglas Space Systems Division of St. Louis, is a diode-pumped, solid-state Cr-Nd-yttrium-aluminum-garnet laser that operates at a wavelength of 1.064 μm and emits 12-ns-long pulses.
13. M. T. Zuber, D. E. Smith, A. F. Cheng, T. D. Cole, *J. Geophys. Res.* **102**, 23761 (1997).
14. T. D. Cole *et al.*, *Space Sci. Rev.* **82**, 217 (1997).
15. Data used herein were obtained at a 1-Hz sampling rate which, combined with the laser beam divergence of 235 μrad, results in surface spot sizes of ~45 m in the 200-km orbit and 11 m in the 50-km orbit. The precision of NLR range measurements approaches the limiting resolution of 31.2 cm on smooth level surfaces and may increase up to ~6 m for spacecraft pointing angles of 20° on a level surface (13, 34).
16. The accuracy of the spot location in latitude and longitude is limited by the knowledge of the spacecraft pointing at ~50 to 100 mrad which corresponds to 1 to 20 m on the surface for ranges of 20 to 200 km, and by spacecraft position uncertainties of up to several hundred meters. The estimate of global topographic accuracy includes contributions from radial orbit error of ~30-m rms and instrument error of 1-m rms at 20-km range. Limitations on the accuracy of our model include the product of the gravitational constant and asteroid mass, *GM* (11), and the long-wavelength terms in the gravity model (Table 1).
17. From the radii data we removed obviously erroneous measurements and rejected others with excessive angles of incidence on the surface. We binned the remaining data in 3° by 3° blocks, weighting all data equally. This binned data set was used to derive a spherical harmonic expansion for the shape of Eros to degree and order 48. The stability of the individual coefficients and the degree variances for solutions of varying degree and order suggested that the solution was robust beyond degree and order 24 (spatial resolution of 957 m). We adopted the 24 by 24 coefficients of the 48 by 48 model as Eros shape model NLR190.
18. J. Veverka *et al.*, *Science* **289**, 2088 (2000).
19. S. J. Ostro, K. D. Rosema, R. F. Jurgens, *Icarus* **84**, 334 (1990). Earth-based observations tend to overestimate asteroid size because if one radar pixel is illuminated, the topography is erroneously modeled to extend to the center of that pixel.
20. P. Thomas, *Icarus* **77**, 248 (1989).
21. S. J. Ostro *et al.*, *Science* **248**, 1523 (1990).
22. S. J. Ostro *et al.*, *Science* **288**, 836 (2000).
23. Supplementary data are available at Science Online at www.sciencemag.org/feature/data/1052631.shl.
24. The COM is determined from the gravity field, chosen so that the origin of the field is (0,0,0). The COF is the geometric center of the asteroid determined from altimetry. For a near-spherical body such as a planet, the offset of the COF from the COM is described by the degree-1 terms of a spherical harmonic expansion of the shape. However, for a complexly shaped body, higher order terms must be taken into account (35).
25. M. R. Cooper, R. L. Kovach, J. S. Watkins, *Rev. Geophys.* **12**, 291 (1974).
26. We assume a linear gradient in the distribution in three cartesian directions ($\vec{x} = x, y, z$) such that $\rho(\vec{r} = \rho_0(1 + \vec{\gamma}\vec{x})$ where ρ is density, ρ_0 is Eros's average density of 2670 kg m⁻³ (11), and $\vec{\gamma}$ is the gradient vector, determined by numerical integration. The composition of Eros is consistent with that of low-

- iron chondrites (29), with measured densities of ~3200 to 3500 kg m⁻³ (36). Meteorite analogs are denser than Eros's bulk density, which suggests that the asteroid exhibits some degree of fracturing and/or porosity.
27. E. Asphaug, S. J. Ostro, R. S. Hudson, D. J. Scheeres, W. Benz, *Nature* **393**, 437 (1998).
 28. A. Fujiwara *et al.*, in *Asteroids*, R. P. Binzel, T. Gehrels, M. S. Matthews, Eds. (Univ. of Arizona Press, Tucson, AZ, 1989), pp. 240–265.
 29. J. Trombka *et al.*, *Science* **289**, 2101 (2000).
 30. K. R. Housen and K. A. Holsapple, *Icarus* **84**, 226 (1990).
 31. A. Fujiwara, *Icarus* **83**, 156 (1991).
 32. Gravity was calculated from the shape model assuming homogeneous density. Centrifugal accelerations due to the asteroid's rotation were taken into account. The gravitational slope is the angle between \hat{g} and $-\hat{n}$, the inward normal, as calculated from a plate representation of a 3° grid of NLR radii in which plates were characterized by areas that differed by up to a factor of 2.
 33. A. Fujiwara, *Icarus* **89**, 384 (1991).
 34. A. F. Cheng *et al.*, *Icarus*, in press.
 35. O. Aharonson and M. T. Zuber, unpublished data.
 36. G. J. Consolmagno and D. T. Britt, *Meteorit. Planet. Sci.* **33**, 1231 (1998).
 37. D. D. Rowlands *et al.*, "GEODYN II System Description" (Hughes-STX Contractor Report, 1993).
 38. J. J. McCarthy *et al.*, "GEODYN Systems Descriptions and Operations Manuals" (NASA Goddard Space Flight Center and Hughes-STX Contractor Report, 1994).
 39. To determine the shape of Eros we used NLR data collected between days 065 and 190 of 2000 during spacecraft orbits with semi-axes (in km) as follows: 200 by 200, 100 by 200, 100 by 100, 100 by 50, and 50 by 50. We analyzed the NLR data in conjunction with the orbital ephemeris of NEAR and computed the orbit of the spacecraft using the GEODYN/SOLVE orbital anal-

ysis programs (37, 38). We determined global topography from a joint inversion of altimetry and Doppler data, which yielded an altimetric model, spacecraft orbits, and a degree and order 5 gravity model, with coefficients through degree 3 given in Table 1. Using our orbits and gravity field and incorporating the pointing data from spacecraft quaternions that yield the attitude and orientation of the spacecraft in inertial space, we estimated the locations of bounce points of the laser pulse on the surface of Eros. Asteroid radii were measured by subtracting ranges from the spacecraft orbit.

40. We thank the NEAR-Shoemaker spacecraft, mission operations, and navigation teams for support. We also thank B. Williams and D. Yeomans for providing tracking data used to calculate the orbits, P. Thomas for helpful discussions, D. Pavlis and J. McCarthy for assistance in tracking data analysis, and M. Nolan for review. The NLR investigation is supported by the NASA NEAR-Shoemaker Project.

30 May 2000; accepted 30 August 2000

The Elemental Composition of Asteroid 433 Eros: Results of the NEAR-Shoemaker X-ray Spectrometer

J. I. Trombka,^{1*} S. W. Squyres,² J. Brückner,³ W. V. Boynton,⁴ R. C. Reedy,⁵ T. J. McCoy,⁶ P. Gorenstein,⁷ L. G. Evans,⁸ J. R. Arnold,⁹ R. D. Starr,¹⁰ L. R. Nittler,¹ M. E. Murphy,¹⁰ I. Mikhcheva,⁴ R. L. McNutt Jr.,¹¹ T. P. McClanahan,¹ E. McCartney,² J. O. Goldsten,¹¹ R. E. Gold,¹¹ S. R. Floyd,¹ P. E. Clark,¹⁰ T. H. Burbine,⁶ J. S. Bhangoo,⁴ S. H. Bailey,⁴ M. Petaev⁷

We report major element composition ratios for regions of the asteroid 433 Eros imaged during two solar flares and quiet sun conditions during the period of May to July 2000. Low aluminum abundances for all regions argue against global differentiation of Eros. Magnesium/silicon, aluminum/silicon, calcium/silicon, and iron/silicon ratios are best interpreted as a relatively primitive, chondritic composition. Marked depletions in sulfur and possible aluminum and calcium depletions, relative to ordinary chondrites, may represent signatures of limited partial melting or impact volatilization.

The Near Earth Asteroid Rendezvous (NEAR)-Shoemaker mission began an orbital rendezvous with the S-type asteroid Eros on 14 February 2000. The x-ray/gamma-ray spectrometer system (XGRS) on NEAR detects 1- to 10-keV x-rays and 0.3- to 10-MeV gamma-ray emissions. Discrete line x-ray and gamma-ray emissions in these energy domains can be used to determine the surface distribution of many geologically important elements (e.g., Mg, Al, Si, S, Ca, Fe, O, K, and possibly Th) (1–3). In addition, NEAR carries a near-infrared spectrometer and a multispectral imager (4–6), allowing direct comparison between the elemental composition measured by the XGRS and the mineralogy inferred from the optical and infrared spectral measurements. These complementary data sets will help elucidate possible relations to known classes of meteorites and pro-

cesses that might have occurred on Eros (e.g., impact metamorphism and partial melting).

Since 2 May 2000, NEAR has been in a low (35- to 50-km) orbit about the center of mass of Eros, beginning an extended phase of detailed surface mapping of the asteroid. Here, we report results from the NEAR x-ray spectrometer (XRS) on the surface composition of Eros. These results are compared to compositions of meteorite groups. Statistically significant results from gamma-ray spectrometry require integration times that are substantially longer than those from x-ray spectrometry results.

Remote sensing x-ray spectroscopy. The x-ray spectrum of a planetary surface measured from orbit is dominantly a combination of the fluorescence excited by incident solar x-rays and coherently and incoherently scattered solar x-rays from the surface. The sampling depth is

dependent on energy, but it is always less than 100 μm for the elements of interest here. The most prominent characteristic x-ray fluorescent lines that can be observed by the NEAR XRS are the $K\alpha$ lines (1 to 10 keV) from the major elements Mg (1.254 keV), Al (1.487 keV), Si (1.740 keV), S (2.308 keV), Ca (3.691 keV), and Fe (6.403 keV). Emission produced by solar and cosmic charged particles is negligible, and astronomical x-ray sources are occulted by the asteroid, which fills the field of view below an altitude of 400 km.

Incident solar x-rays provide the excitation source for x-ray generation from a planetary surface. Thus, knowledge of the solar spectrum is critical to obtaining quantitative analyses (7, 8). The solar flux from 1 to 10 keV is composed of a continuum and discrete lines. Theoretical models predict the solar spectrum as a function of solar activity (9–12). Solar intensity decreases by three to four orders of magnitude from 1 to 10 keV, so fluorescent lines and scatter-induced background radiation exhibit greater intensity at lower energies. As solar activity increases, the spectra harden, with increased output at higher energies, reduced steepness in the spectral slope, and increased overall x-ray

¹Goddard Space Flight Center, Code 691, Greenbelt, MD 20771, USA. ²Space Sciences Building, Cornell University, Ithaca, NY 14853, USA. ³Max-Planck-Institut für Chemie, Postfach 3060, D-55020 Mainz, Germany. ⁴Department of Planetary Science, Space Sciences Building, University of Arizona, Tucson, AZ 85721, USA. ⁵Los Alamos National Laboratory, NIS-2, MS-D436, Los Alamos, NM 87545, USA. ⁶Department of Mineral Sciences, National Museum of Natural History, Smithsonian Institution, Washington, DC 20560–0119, USA. ⁷Smithsonian Astrophysical Observatory, 60 Garden Street, MS-4, Cambridge, MA 02138, USA. ⁸System Sciences Division, Computer Sciences Corporation, 1100 West Street, Laurel, MD 20707, USA. ⁹University of California, San Diego, Chemistry BC-017/Cal Space 0524, 9500 Gillman Drive, La Jolla, CA 92093, USA. ¹⁰Physics Department, Catholic University of America, 620 Michigan Avenue NE, Washington, DC 20064, USA. ¹¹Applied Physics Laboratory, Johns Hopkins University, Johns Hopkins Road, Laurel, MD 20723, USA.

*To whom correspondence should be addressed.